Supplementary Information

Curvature-optimised multilevel SERS substrates formed by femtosecond laser shaping based on electrons dynamics control

Jianqi Dou[1], Lan Jiang[1,2,3,*], Xiaowei Li[1,2], Xibiao Li[1,4], Yanfeng Li[1], Zhi Wang[1], Andong Wang[1], Xiangyu Zhang[1], Yifan Wang[1], Yunxia Zhao[1,5], Le Dai[1,5]

[1] Laser Micro/Nano Fabrication Laboratory, School of Mechanical Engineering, Beijing Institute of Technology, No. 5 Zhongguancun South Street, Beijing 100081, China

[2] Yangtze Delta Region Academy of Beijing Institute of Technology, No. 1940 Dongfang North Road, Jiaxing 314019, Zhejiang Province, China

[3] Beijing Institute of Technology Chongqing Innovation Center, No. 1 Mingli Road, Chongqing 401120, China

[4] Institute of Modern Optics, Nankai University, Tianjin Key Laboratory of Micro-scale Optical Information Science and Technology, No. 94 Weijin Road, Tianjin 300350, China

[5] School of Optics and Photonics, Beijing Institute of Technology, Beijing 100081, No. 5 Zhongguancun South Street, China

Keywords: Temporally-shaped femtosecond laser, surface-enhancement Raman scattering, microlens, wrinkles, Ag nanoparticles, pesticide residue detection

This PDF file includes:

Figure S1 to S11, Table S1

Part S1: Raman spectra of the modified region irradiated by Gaussian double-pulse laser

The two peaks observed at 495 cm^{-1} and 606 cm^{-1} represent three-membered and four-membered ring structures, respectively. However, since the D1 band is located in close proximity to the dominant main peak (centered at ~450 cm^{-1}), its intensity can be influenced by spectral overlap. Therefore, variations in the intensity of the D2 band are selected as a more reliable indicator to quantify the extent of material modification. The integrated area between the D2 Raman band and the fitted baseline is used to represent its intensity.

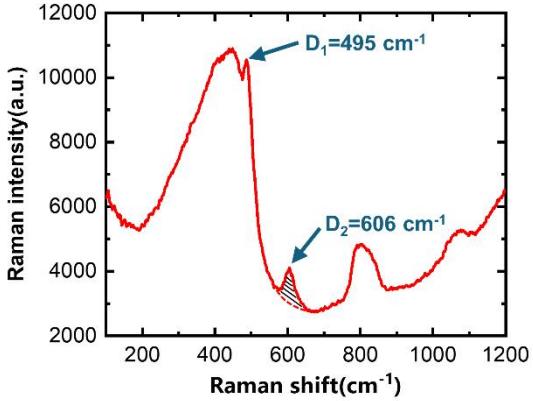

Figure S1 Raman spectra of the modified region.

Part S2: Schematic of microlens etching with different curvatures

Etch the laser-modified fused silica using 40% HF solution (volume fraction). During etching, the modified regions were preferentially removed. Due to differences in etching efficiency between the radial and depth directions, different modification depths are ultimately transformed into varying curvatures of the microlens. The curvature was calculated as follows:

$$\varepsilon = \frac{1}{R} = \frac{8H}{D^2 + 4H^2}$$

Here, ε denotes the curvature, R is the radius of curvature, D is the microlens diameter, and H is the microlens height. Microlens with greater heights exhibit larger curvatures, indicating that deeper modification results in higher curvature.

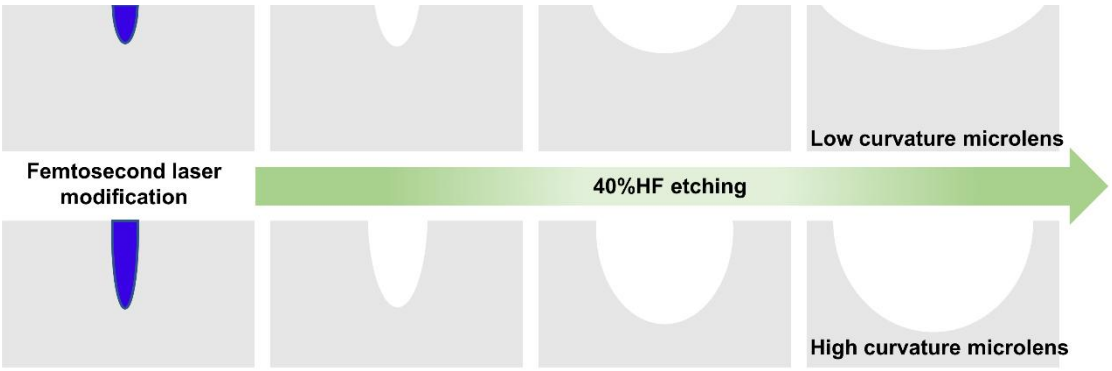

Figure S2 Schematic of micro-lens etching with different curvatures

Part S3: Optical microscope images of etching process of high-curvature/low-curvature microlens

Microlens with different modification levels require different etching time to reach the same size. With double-pulse delay of 10 ps, etching to 60 μm diameter takes 4 h, whereas 300 ps delay requires 10 h. Regions with higher modification levels etch faster due to a greater presence of three-membered and four-membered rings in the modified areas.

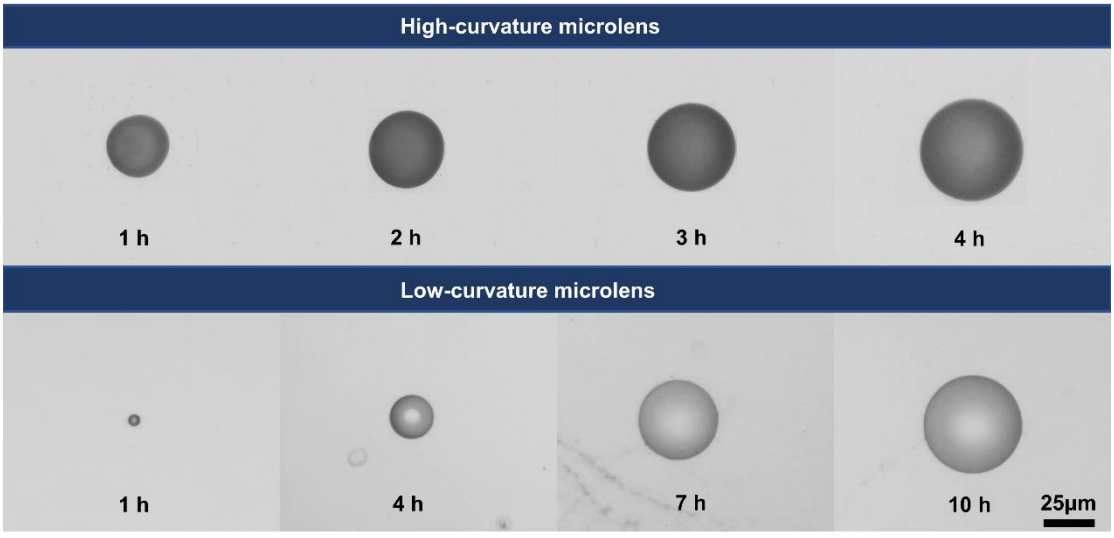

Figure S3 optical microscope images of etching process of high-curvature/low-curvature microlens

Part S4: Confocal microscope image of high-curvature microlens array template

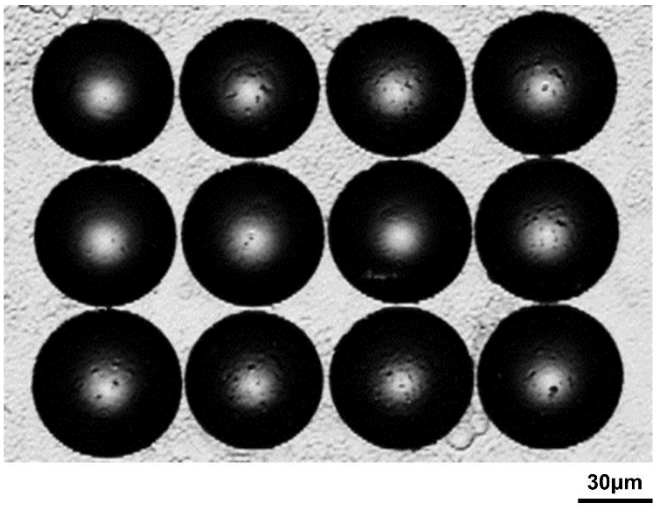

Figure S4 Confocal image of high-curvature microlens array template.

Part S5: Statistical distribution of Ag nanoparticle size

Use laser particle size analyzer to analyze the particle size of the synthesized AgNPs. The nanoparticle solution was centrifuged at 15,000 rpm for 10 minutes, and remove the supernatant. The precipitate was redispersed in deionized water by ultrasonication for three times. The results show that the AgNPs mainly range from 40 to 60 nm in diameter. Such small particle sizes play a critical role in enhancing the local electric field.

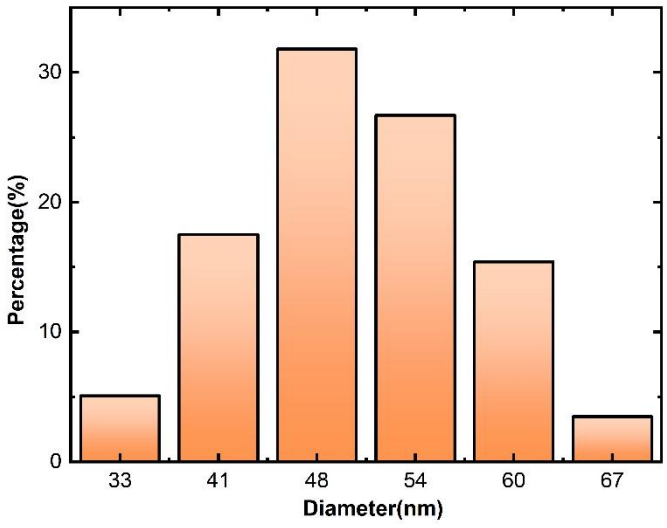

Figure S5 Statistical distribution of Ag nanoparticle size

Part S6: FDTD-simulated electric field distributions of different structures.

FDTD simulations were extended to different structural designs to investigate the enhancement of curvature and structural optimization. Figures S6(a1) - (d1) show the electric field distributions of microlens with varying curvatures. As summarized in Figure S6(f), the electric field intensity above the structures slightly increase with curvatures. Similarly, the electric field distributions of wrinkled microlens at varying curvatures are shown in Figures S6(a2)–(d2) and the corresponding intensities are quantified in Figure S6(g). The enhancement is comparable to that of a single microlen. Figure S6(e) provides a statistical comparison of the electric field intensities for the different structures in Figure 4(a). The result reveals that SERS substrates with combined curvature and structural optimization achieve markedly superior performance, whereas the enhancement is limited in the absence of AgNPs. These findings demonstrate that the coupled effect between the plasmonic “hot spots” provided by AgNPs and the enhanced electromagnetic fields induced by the optimized microstructures makes superior performance.

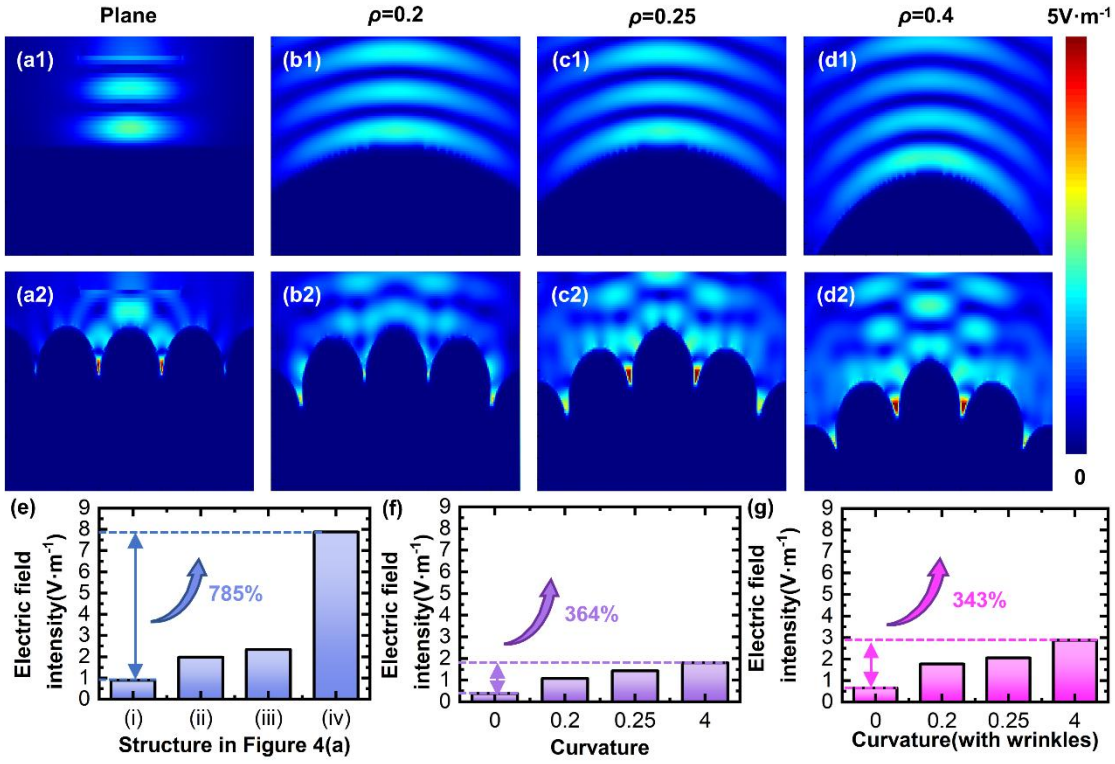

Figure S6 FDTD-simulated electric field distributions for the different structures. (a1) - (d1) Single microlen with different curvatures. (a2) - (d2) Wrinkles and microlens with different curvatures. (e) - (g) Statistical analysis of the electric field distributions above different structures in Figure 4a, Figure(a1) - (d1), and Figure (a2) - (d2) respectively.

Part S7: The SERS spectra (R6G) with a concentration of 10^{-11}M and linear fitting between concentration and SERS intensity in log scale

Figure S7(a) depicts the SERS spectra of R6G at a concentration of 10^{-11} M. When the concentration of R6G is decreased to 10^{-11} M, the weak signal intensity results in a low signal-to-noise ratio, leading to minor peak shifts during spectral fitting. Therefore, the lower detection limit of our method is 10^{-11} M. Figure S7(b) presents the linear fitting between the analyte concentration and the corresponding SERS intensity. The substrate exhibited robust SERS performance over a range of analyte concentrations.

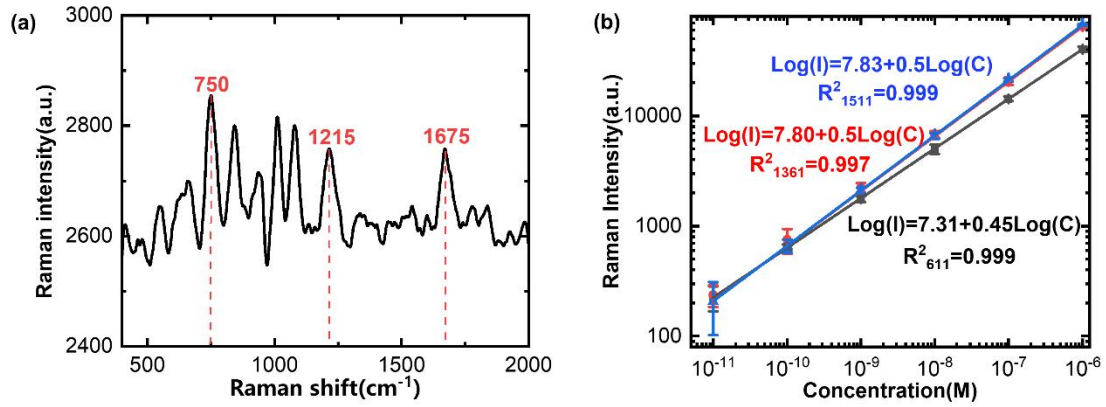

Figure S7 (a) The SERS spectra (R6G) with a concentration of 10^{-11}M. (b) linear fitting between concentration and SERS intensity in log scale.

Part S8: Comparison with the reported flexible SERS substrate

Figure S8 presents a comparison of different SERS substrates featuring micro-nano composite structures with Ag nanoparticles. The comparison is primarily made in terms of analyte, detection limit, and enhancement factor in Table S1.

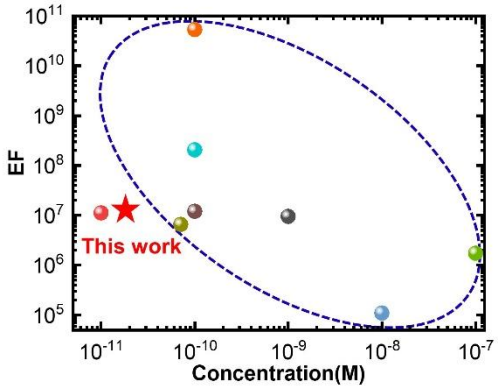

Figure S8 Comparison of the limit of detection concentration and the enhancement factor (EF) achieved in this work with those reported in other studies [38-44].

Table S1. Comparison with the reported flexible SERS substrate

SERS substrate	Analytes	Limit of detection	Enhancement factor	Ref.
The AgNPs@β-AgVO3-NRs substrate	Chloramphenicol (CAP)	1×10^{-10}M	2.05×10^{8}	38
The AgNPs@PDA@MNs substrate	R6G	1×10^{-10}M	1.2×10^{7}	39

The AgNWs/PDMS substrate	R6G	7.06×10^{-11}M	6.6×10^{6}	40
The NPR-Ag substrate	CV	1×10^{-10}M	5.33×10^{10}	41
The PDMS@PDA@AgNPs substrate	CV	1×10^{-8}M	1.1×10^{10}	42
The AuNPs@PDA@PMMA-MN substrate	R6G	1×10^{-7}M	1.74×10^{6}	43
The AgNPs@GS substrate	CV	1×10^{-9}M	9.53×10^{6}	44
The curvature optimized multilevel SERS substrate	R6G	1×10^{-11}M	1.12×10^{7}	This work

Part S9: Raman spectra of the SERS substrate under different stress states

Flexibility plays a crucial role to improve the portability of SERS substrates and enhance adhesion to curved surfaces. PDMS, with its excellent elasticity and biocompatibility, serves as the excellent substrate material. We stretched, bent, and twisted the fabricated SERS substrates, and then tested their SERS performance to demonstrate their mechanical adaptability.

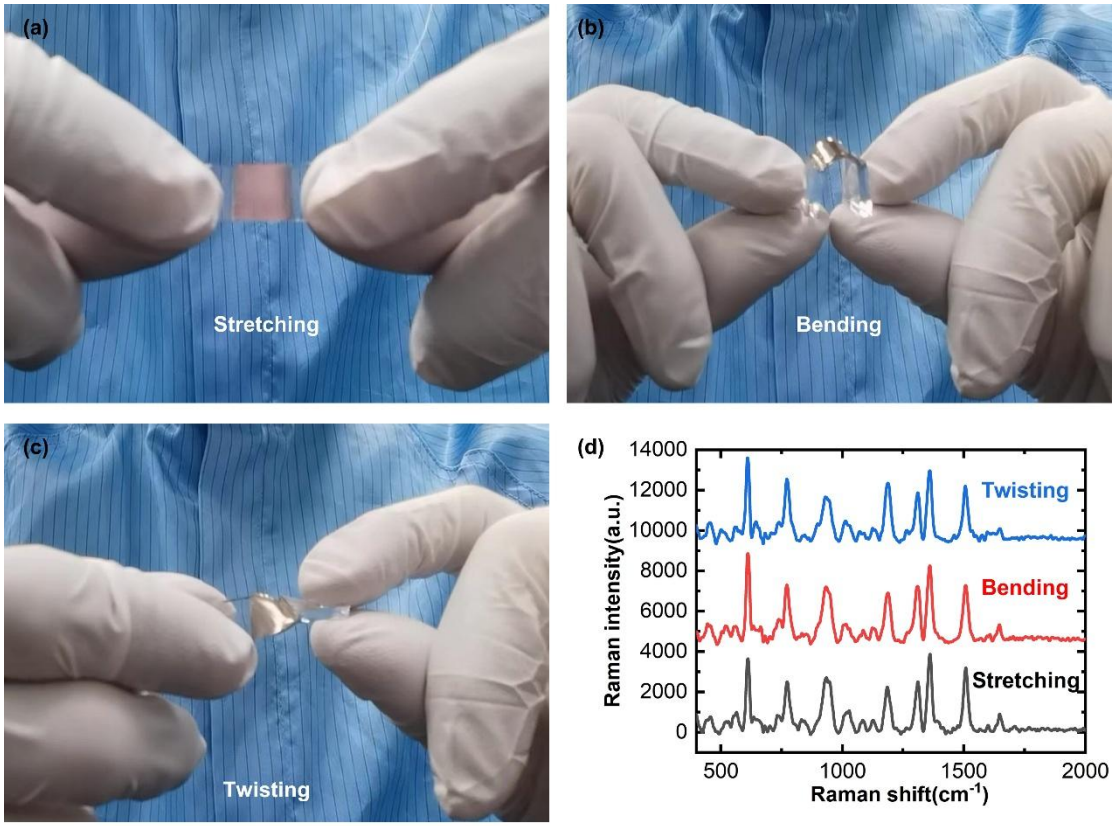

Figure S9 Raman spectra of the SERS substrate under different stress states.

Part S10: Pictures of the wrinkle stretching apparatus

Inside the magnetron sputtering system, the sample was fixed on a one-dimensional translation stage, and strain was applied via the motion of a lead screw. Gold film was then deposited onto the strained sample through magnetron sputtering. After the deposition, the sample and translation stage were removed, and the applied strain was released, resulting in the formation of surface wrinkle structures on the sample.

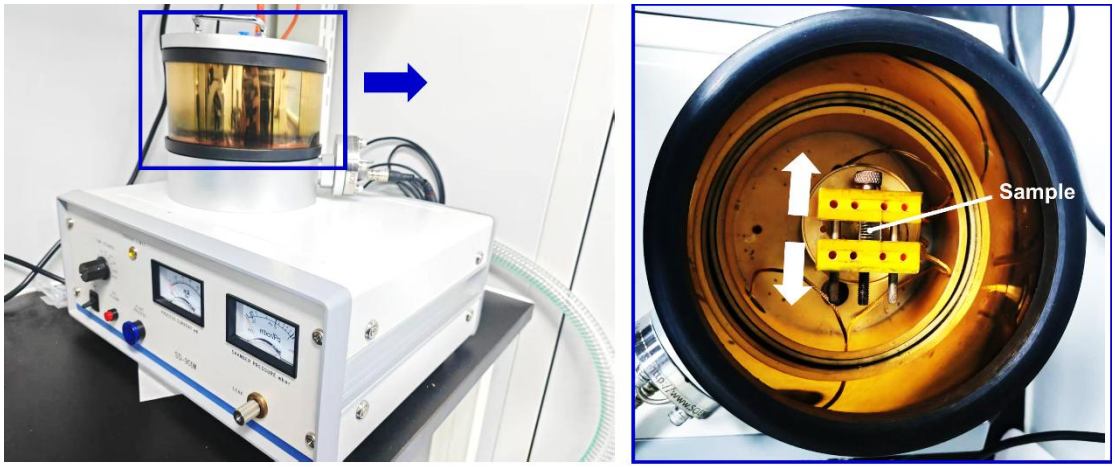

Figure S10 Pictures of the wrinkle stretching apparatus.

Part S11: The AFM images of wrinkle morphology.

The wrinkle morphology was characterized using atomic force microscopy (AFM). Regional scans were performed on both the microlens surface and the substrate surface. The extracted cross-sectional profiles reveal that The wavelength of on-microlen wrinkles and off-microlen wrinkles are 4.4 μm and 4.8 μm, while the height are 1.25 μm and 1.33 μm.

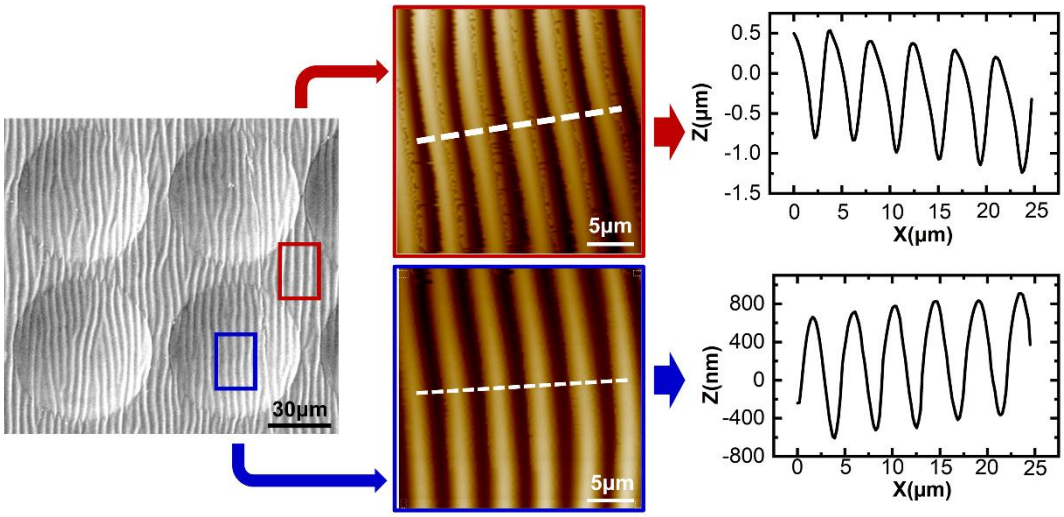

Figure S11 The AFM images of wrinkle morphology.